RESEARCH ARTICLE

NANO · MICRO small
www.small-journal.com

Enzyme-Assisted Selective Biosynthesis of Polyrotaxane Assemblies in Living Cells for Precision Supramolecular Phototherapy

Ya-Hui Song, Zhuo Lei, Ze-Kai Deng, Bing Hu, Guang-Ming Liu, Ying-Ming Zhang, Yong Chen, Zhilin Yu, and Yu Liu**

In contrast to conventional bottom-up self-organization in an abiotic environment, it remains a formidable challenge to construct mechanically interlocked and biologically active supramolecules in cells and organisms. Notably, the in-situ formation of polyrotaxane-type nanoarchitectures has not been reported, and their biological implication is unexplored. Here, it is report the first selective biosynthesis of polyrotaxane assemblies in living cells for combined tumor therapy. Four-armed porphyrins appended with lysine and glutamine residues are enzymatically coupled via overexpressed transpeptidase in malignant cells. The robust host–guest complexation between permethylated β-cyclodextrin and porphyrin not only drives the morphological conversion from disordered polymers to 2D polyrotaxanes, but also improves the structural integrity and photophysical performance of porphyrin scaffolds. The chemical modification of the cyclodextrin skeleton further enables the biofunctional diversification of intracellularly formed polyrotaxanes, as demonstrated by the covalent incorporation of a targeting motif and photoactivable prodrug for specific cytoskeletal disruption. The obtained polyrotaxane assemblies exhibit efficient singlet oxygen generation up to 221% and prolonged tumor retention over 120 h, resulting in elevated photocytotoxicity and effective suppression of cell dissemination under light irradiation. The findings establish a unique in-cellulo assembling evolution for attaining topologically complex supramolecules and demonstrate an in-situ nanoformulation of biomedical agents in disease theranostics.

1. Introduction

A living cell is a sophisticated biological factory and a natural matter/energy reservoir where diverse biochemical reactions occur in a spatiotemporally ordered manner.[1–7] Nowadays, the creation of innovative nanomedicines and biotechnology increasingly relies on the cell-based synthetic methodology, which will surely provide bountiful opportunities to interface with chemistry and biology.[8–11] Among the biocompatible chemical reactions in living systems, in-cellulo polymerization is regarded as one of the most feasible and reliable means in attaining complex yet ordered nanostructures, ranging from naturally occurring biomacromolecules (e.g., DNA, RNA, and polysaccharides) to artificially synthetic assemblies (e.g., metallic nanoparticles,[12,13] amphiphilic assemblies,[14,15] and linear polymers,[16–19] **Scheme 1a**). Taking malignant cells as an example, the pathophysiological hallmarks, including acidic pH,[20] redox dysregulation,[21–23] and aberrant enzymatic expression,[24–26] can be fully utilized as chemical additives and catalysts to trigger polymerization reactions in these specific cells and allow us to fabricate stimuli-responsive antitumor bioagents. Remarkably, more evidence has revealed that the in-situ formation of polymeric species within living cells can induce high-efficiency molecular accumulation and suppress efflux-mediated drug resistance, thereby advancing drug-free therapies. Therefore, it is of paramount importance to precisely manipulate the biosynthetic evolution of in-situ supramolecular

Y.-H. Song, Z. Lei, Z.-K. Deng, B. Hu, Y.-M. Zhang, Y. Chen, Y. Liu
College of Chemistry
State Key Laboratory of Elemento-Organic Chemistry
Collaborative Innovation Center of Chemical Science and Engineering (Tianjin)
Nankai University
Tianjin 300071, P. R. China
E-mail: ymzhang@nankai.edu.cn; yuliu@nankai.edu.cn

The ORCID identification number(s) for the author(s) of this article can be found under https://doi.org/10.1002/smll.202511673

DOI: 10.1002/smll.202511673

G.-M. Liu
Department of Urology
Tianjin First Center Hospital
Nankai University
Tianjin 300071, P. R. China

Z. Yu
Key Laboratory of Functional Polymer Materials
Ministry of Education
State Key Laboratory of Medicinal Chemical Biology
Institute of Polymer Chemistry
College of Chemistry
Nankai University
Tianjin 300071, P. R. China

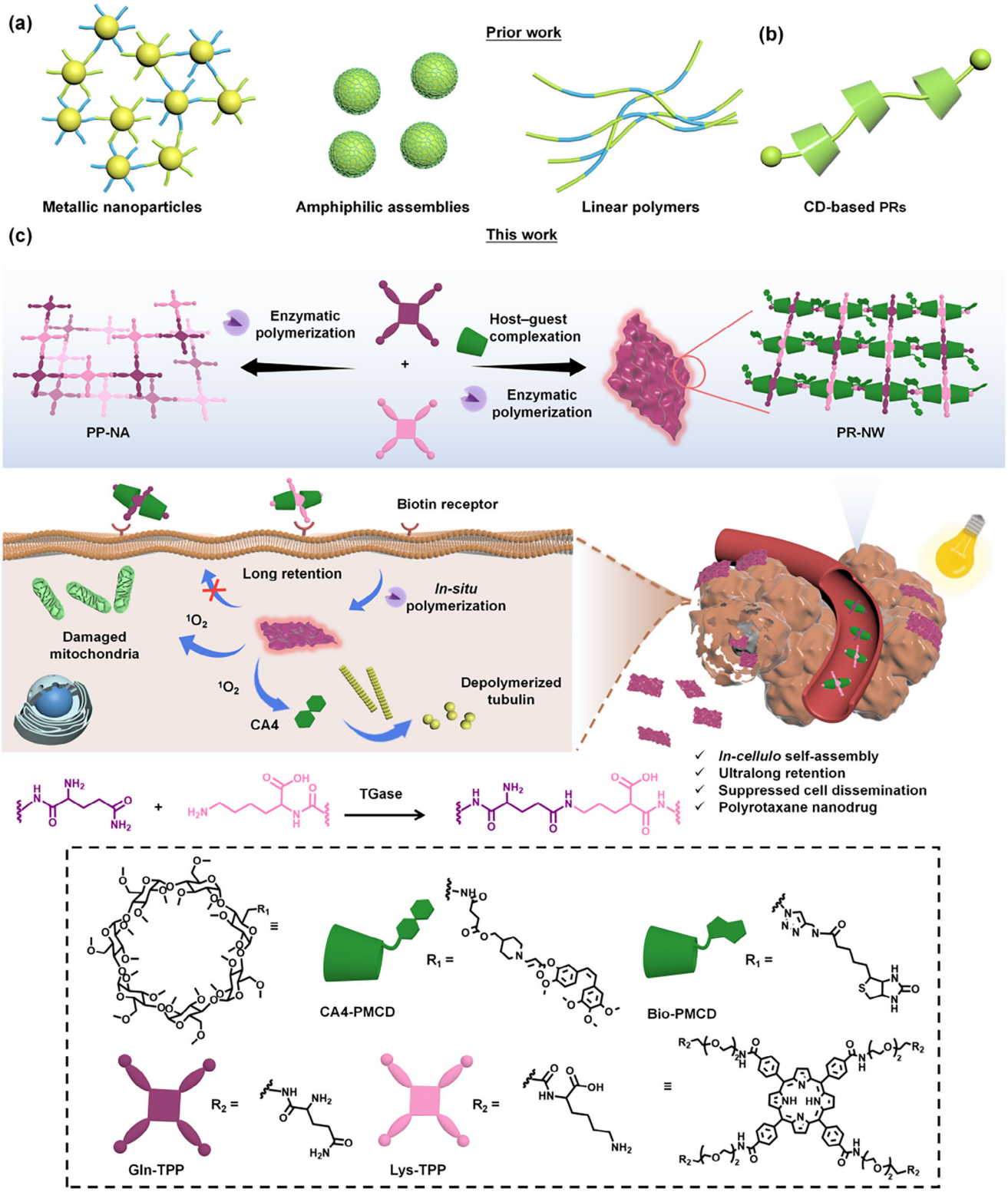

Scheme 1. a) Reported in-cellulo polymerization with different morphologies; b) Typical structure of CD-threaded polyrotaxane with bulky stoppers; c) Schematic illustration of in-situ assembly of polyrotaxane assembly fabricated by host–guest complexation and enzymatic polymerization and their biological consequence, as well as the molecular structures of used PMCD and TPP derivatives.

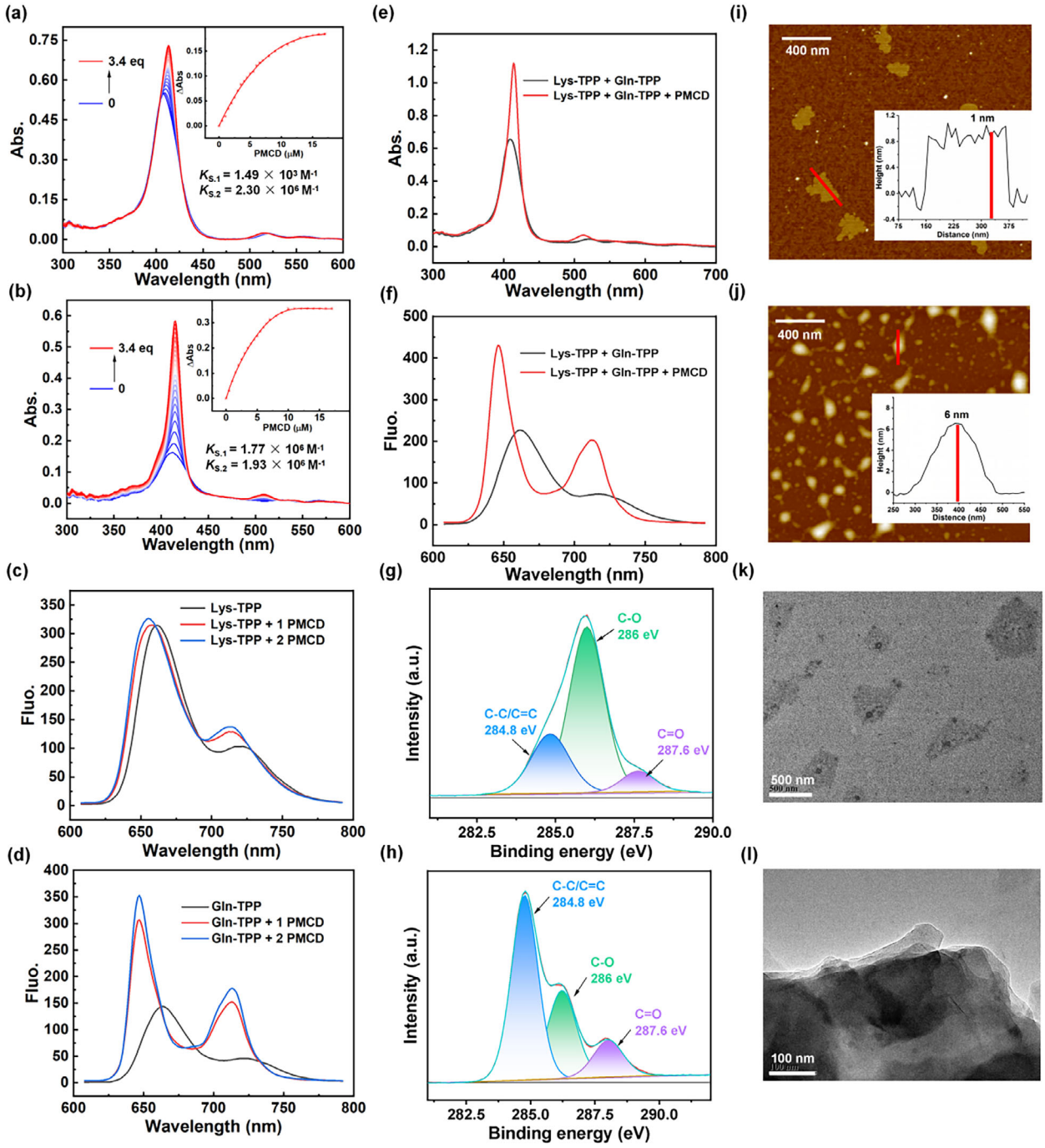

Figure 1. UV–vis spectral titration of a) Lys-TPP⊂PMCD and b) Gln-TPP⊂PMCD complexation in PBS; Inset: calculation of the K_S values by the nonlinear least-squares curve-fitting method ([Lys-TPP] = [Gln-TPP] = 5 μM, and [PMCD] = 0–17 μM); Fluorescence emission spectra of c) Lys-TPP and d) Gln-TPP before and after addition of PMCD ([Lys-TPP] = [Gln-TPP] = 10 μM, and [PMCD] = 10 and 20 μM); e) UV–vis absorption and f) fluorescence emission spectra of TPP monomers and complex monomers; XPS spectra of g) PR-NW and h) PP-NA; and i,j) AFM and k,l) TEM images of i,k) PR-NW and j,l) PP-NA.

assemblies at the cellular level and efficiently produce biomimetic materials with exceptional topological structures and biological performance.[27–30]

In the realm of supramolecular chemistry, the emergence of mechanically interlocked molecules with unique topological features, such as (poly)rotaxanes, catenanes, and molecular knots, has greatly expanded the research scope for biomedical and material science.[31–38] In this regard, cyclodextrin-based polyrotaxanes (CD-based PRs), a family of promising end-capped supramolecules consisting of cyclic saccharides as

wheels and polymer chains as axles, with highly complementary molecular mobility and constraint, have inventive applications in supramolecular theranostics and healthcare monitoring (Scheme 1b).[39–42] On one hand, superior to discrete small-molecule components, active ingredients are restrictedly constrained in the polymeric domain, thus avoiding complex pharmacokinetics and uncertain curative outcomes arising from premature release and non-targeted disassociation. On the other hand, superior to the classic polymeric species with robust covalent linkage, the movable ring molecules can slide back and forth along the polymer chain to dynamically initiate their conformational transition in response to environmental variations, thus enabling the generation of self-adaptive biomaterials for drug and gene delivery, and tissue engineering. Nevertheless, compared to the large-scale chemical synthesis in an abiotic environment and the prior use of well-prepared polyrotaxanes in cell incubation and intralesional injection, the precision biosynthesis of polyrotaxane-type nanoarchitectures in living organisms is rarely reported, and their corresponding biological consequence is largely unexplored, to the best of our knowledge.

Combining the intrinsic merits of intracellular polymerization methodology and mechanical interlocking topology, we herein report a selective biosynthesis of highly periodic polyrotaxane assembly in the tumor microenvironment (Scheme 1c). Four-armed tetraphenylporphyrin (TPP) derivatives containing lysine (Lys) and glutamine (Gln) residues were designed and synthesized, which underwent enzymatically coupling reactions in the presence of overexpressed transglutaminase (TGase) in cancer cells. More strikingly, the extraordinarily strong host–guest complexation between permethylated β-cyclodextrin (PMCD) and porphyrin core can not only facilitate the morphological conversion from randomly stacked polymeric aggregates to highly ordered 2D polyrotaxanes, but also enhance the structural integrity and the photodynamic properties of porphyrin scaffolds. The covalent incorporation of biotin as a cell-targeting agent and photoactivatable combretastatin A4 (CA4) as a cytoskeleton-destabilizing prodrug into the PMCD's skeleton can further confer biofunctional diversity to the resultant polyrotaxane assembly, synergistically resulting in the suppression of tumor cell dissemination and invasion for precision supramolecular phototherapy. Overall, this is the first demonstration that the enzyme-activated biosynthetic assembly boosted by host–guest complexation makes topologically interlocked supramolecules a multifunctional nanoplatform for disease therapy.

2. Results and Discussion

2.1. Synthesis and Characterization of Polyrotaxanes In Vitro and in Cell Lysate

Two precursors in the TGase-mediated coupling reaction, lysine- and glutamine-modified tetraphenylporphyrins (Lys-TPP and Gln-TPP), were synthesized via amide condensation, and their chemical structures were comprehensively characterized (Figures S1–S6, Supporting Information). The alkoxy linker in suitable length could increase the water solubility of the whole porphyrin guests and, more importantly, adjust the intermolecular distance between two adjacent porphyrin cores to accommodate a PMCD unit. Meanwhile, the biotinylated PMCD (Bio-PMCD) was synthesized via the Cu(I)-catalyzed azide/alkyne cycloaddition, and the CA4-modified PMCD (CA4-PMCD) bearing a singlet oxygen ($^1O_2$)-cleavable aminoacrylate group was obtained by the esterification with carboxylated PMCD (Figures S7–S12, Supporting Information).

The molecular binding behaviors between PMCD and two TPP-derived monomers, Lys-TPP and Gln-TPP, were primarily studied by spectroscopic titration in phosphate buffer solution (PBS, **Figure 1a,b**). Having validated the 2:1 binding stoichiometry by Job plots (Figure S13, Supporting Information), the binding constants (K_S) were accordingly determined by the spectral changes in UV–vis absorbance. The results showed that the stepwise K_S values of PMCD with Lys-TPP were calculated as 1.49×10^3 and 2.30×10^6 M^{-1}, respectively, and $K_{S,1} = 1.77 \times 10^6$ and $K_{S,2} = 1.93 \times 10^6$ M^{-1} were obtained in the case of Gln-TPP⊂PMCD complexation. Meanwhile, the addition of PMCD could enhance and narrow the S-band absorption of the TPP core, accompanied by a bathochromic shift to some extent. These phenomena indicate that free porphyrins adopted H-type aggregation in aqueous solution, while PMCD effectively inhibited their intermolecular aggregation through host–guest interactions.[43,44] However, Lys-TPP alone gave much stronger UV–vis absorption than Gln-TPP at 410 nm, but the complexation-induced spectral changes of Gln-TPP was more dramatic than the ones of Lys-TPP. This suggests that Gln-TPP could self-aggregate in a more compact form than Lys-TPP in solution under the same experimental conditions, because the latter possess ing both positively charged amino groups and negatively charged carboxyl groups in its long and flexible side chains may form loose zwitterionic aggregates via the electrostatic attraction around porphyrin cores at pH 7.2 in PBS. To quantitatively compare their aggregation behaviors, the aggregation constant (K_{agg}) of Gln-TPP in PBS was readily determined as 1.4×10^4 M^{-1} through nonlinear least-squares regression analysis of concentration-dependent UV–vis spectral changes using the isodesmic (equal-K) model. In contrast, no reliable constant was obtained in the case of Lys-TPP (Figure S14, Supporting Information). Meanwhile, similar changes were also observed in the fluorescence emission spectra (Figure 1c,d); that is, as for the Gln-TPP⊂PMCD complexation, there was a 2.5-fold enhancement in intensity with a pronounced 17-nm hypochromatic shift, whereas the intensity was basically unchanged in the case of Lys-TPP⊂PMCD complexation with a slight hypochromatic shift (6 nm). In addition, an obvious nuclear Overhauser effect (NOE) correlation was found upon complexation with TPP cores, again corroborating the strong intermolecular communication inside the PMCD's cavity (Figure S15, Supporting Information).

Transglutaminase (TGase), one of the characteristic enzymes highly overexpressed in tumor tissues and closely related to the metastasis of cancer cells, can catalyze an amine exchange reaction between the γ-carboxamide group of glutamine residues and the ε-amino group of lysine residues, leading to the intra- or intermolecular crosslinking of the corresponding proteins.[45] In our case, the PMCD-involved polyrotaxane network (PR-NW) using two host–guest complexes and its corresponding porphyrin-based PMCD-free nanoaggregates (PP-NA) using two individual TPP monomers were obtained by the TGase-catalyzed

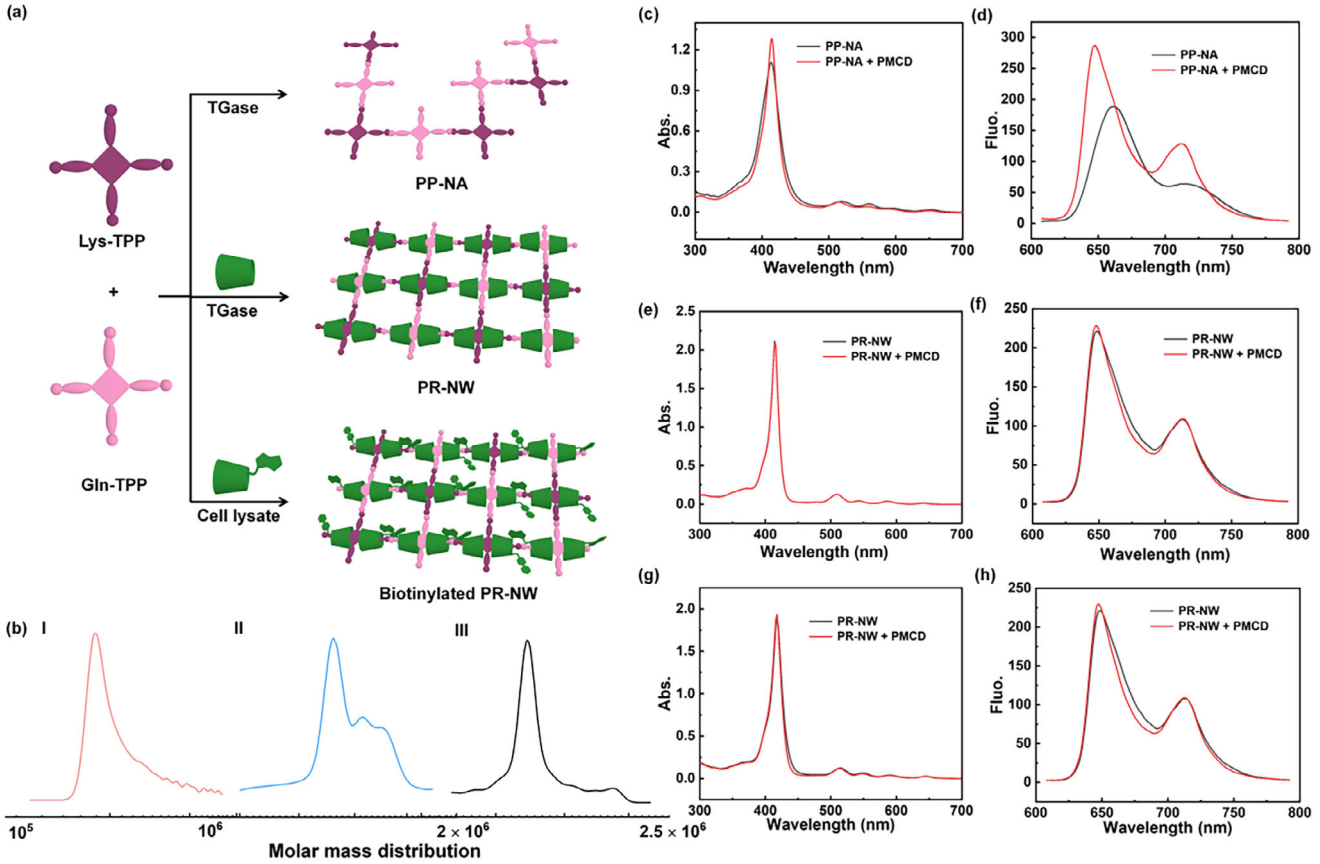

Figure 2. a) Schematic illustration of the formation of PR-NW and PP-NA under different conditions; b) Molecular mass distribution of I) PP-NA, (II) PR-NW, and (III) biotinylated PR-NW by GPC analysis; c,e,g) UV–vis absorption and d,f,h) fluorescence emission spectra of c,d) PP-NA, e,f) PR-NW obtained by disembodied TGase, and g,h) biotinylated PR-NW obtained in cell lysate, respectively, with excess amount of PMCD.

coupling reaction in 4-(2-hydroxyethyl)piperazine-1-ethanesulfon (HEPES) buffer at 37 °C for 24 h in yields of 29.3% and 40.5%, respectively (**Figure** 2a). After completing a full dialysis treatment, molecule weight (M_W), degree of polymerization (DP), and polydispersity (PDI) of PR-NW and PP-NA were measured by gel permeation chromatography (GPC). As depicted in Figure 2b, the M_W value of PR-NW was determined as 6.65 × 10^5, which was 25 times higher than that of PP-NA (2.62 × 10^4). Meanwhile, the PMCD-assisted polymerization also showed a remarkable increase in the DP value from 7 to 178. The increased DP of PR-NW is attributed to the favorable host–guest encapsulation by PMCD, which may enhance the whole molecular rigidity and facilitate the spatial contact between the active center of TGase and the porphyrin substrates.

The polymerization reaction was also monitored by NMR spectroscopy, and the disappearance of the characteristic signals at 6.95 and 7.49 ppm, corresponding to two amide protons of glutamine, also confirmed the occurrence of the polymerization reaction (Figure S16, Supporting Information). By comparing the integrated areas of the porphyrin's aromatic protons and the 1-H in PMCD, the molar ratio of PMCD to porphyrin in PR-NW could be calculated as ≈2:1, which was consistent with the host–guest binding stoichiometric results. In addition, the X-ray photoelectron spectroscopy (XPS) results also demonstrated that the C–O content in PR-NW was significantly increased due to the oxygen-rich functional groups in PMCD (Figure 1g,h).

After the successful synthesis of polymeric assemblies by disembodied TGase, the photophysical properties of PR-NW and PP-NA were comparatively investigated. Strikingly different from PP-NA, the PMCD units in PR-NW could simultaneously enhance UV–vis absorbance and fluorescence emission intensity. Combined with the spectroscopic results of Lys-TPP and Gln-TPP monomers in Figure 1e,f, the existence of PMCD in PR-NW could greatly suppress the π-stacking interaction of porphyrin cores. Moreover, upon continuous light irradiation at 420 nm, the UV–vis absorbance and fluorescence emission intensity of two TPP monomers significantly decreased. In contrast, the negligible spectral changes in PR-NW suggest that the host–guest complexation with PMCD significantly enhanced the photostability of TPP (Figures S17 and S18, Supporting Information). In addition, compared to two TPP monomers, the decline in UV–vis absorption and fluorescence emission of PP-NA became smaller, implying that the cross-linked polymerization also contributes to the photostability enhancement to a certain extent.

Furthermore, the structural integrity of PR-NW and PP-NA was comparatively examined by switching the used solvents. First, when the purely organic solvent (CH_2Cl_2) was used to dissolve PMCD, free host–guest complexes would be completely disassembled because of the loss of hydrophobic interaction.

Next, as illustrated in Figure 2c–f, no significant change was observed in the UV–vis absorption and fluorescence emission spectra upon re-addition of PMCD to an aqueous solution of PR-NW, whereas distinct variation was observed in the spectra of PP-NA. This observation clearly indicated that the polymeric aggregates formed by PP-NA possessed a substantial number of structural defects with exposed porphyrin sites arising from inefficient polymerization, which could be encapsulated by excess PMCD in water. In contrast, due to the complexation-enhanced structural rigidity, PR-NW gave a higher degree of end-capping efficiency with satisfactory integrity and periodicity.

The molecular assembling morphology was intuitively characterized by atomic force microscope (AFM) and transmission electronic microscope (TEM) experiments. AFM images showed the formation of lamellar structures in PR-NW with an average height of 1.0 nm, which was basically consistent with the external diameter of PMCD (0.8 nm, Figure 1i). In addition, the height of PP-NA increased to 6 nm, corresponding to the intermolecularly π-stacked nanoaggregates (Figure 1j). Meanwhile, TEM images also confirmed the TPP monomers mainly formed amphiphilic nanoparticles, whereas PR-NW and PP-NA gave monodisperse nanosheets and amorphous aggregates, respectively (Figure 1k,l; Figure S19, Supporting Information). Meanwhile, the Zeta potentials of both two TPP monomers and the TGase-catalyzed polymeric assemblies are close to zero, which is mainly attributed to the charge neutralization between the negatively charged carboxyl groups on Lys-TPP and the positively charged amino groups on Gln-TPP (Figure S20, Supporting Information).

Furthermore, to bridge the gap between aqueous buffer solution and the living cellular environment, cell lysate was further used as a reaction medium to mimic the intricate composition and properties of components inside the cells (Figure 2a).[46] In this case, a large number of Hela cells was collected and broken down by ultrasonication, followed by the addition of two biotinylated TPP-containing inclusion complexes as monomers. As expected, highly polymeric species were observed in the cell lysate with the M_W value of 1.83×10^6 by GPC analysis, which was in accordance with the data obtained in HEPES (Figure 2b). This result also substantiates that the host–guest complexes are quite stable and biocompatible for polyrotaxane formation despite the overcrowded conditions of the lysate. Similarly, the structural information of the obtained PR-NW was explored by the spectroscopic and microscopic methods, suggesting that the structural integrity could be maintained in cell lysate (Figure 2g,h).

2.2. ROS Generation, Photocytotoxicity, and Light-Activated Drug Release

Then, the cell uptake by tumor and normal cells was comparatively examined by using Bio-PMCD, and flow cytometry was employed for dynamic monitoring of cell-uptake efficiency. As discerned in **Figure 3**a,b; Figure S21 (Supporting Information), after incubation for 24 h, the uptake ratios of biotinylated complex monomers (Lys-TPP⊂Bio-PMCD and Gln-TPP⊂Bio-PMCD) in Hela and MCF-7 cells reached up to 20.3% and 40.7%, respectively, while the 293T cells exhibited a negligible uptake efficiency of only 1.2% with statistically significant differences among three groups, substantiating that the biotinylation of PR-NW could clearly distinguish cancer cells from normal ones. Confocal laser scanning microscopy (CLSM) images also revealed that when treated by two biotinylated complex monomers, stronger red fluorescence was exclusively observed by efficient internalization in the Hela and MCF-7 cells. In the control experiment, in the absence of Bio-PMCD, red fluorescence was extensively distributed in both normal and cancer cells upon incubation merely with TPP monomers (Lys-TPP and Gln-TPP, Figure 3c).

On account of the photosensitive porphyrin arrays in PR-NW and PP-NA, 9,10-anthryl-bis(methylene)dimalonic acid (ABDA) was employed as an indicator for singlet oxygen ($^1O_2$) and the corresponding $^1O_2$ quantum yields were calculated by fitting the UV absorbance at 378 nm plotted against time (Figure 3d; Figures S22 and S23, Supporting Information). As presented in Table S1 (Supporting Information), the $^1O_2$ quantum yields of PP-NA and PR-NW were obtained as 116% and 221%, respectively, once again demonstrating the significant enhancement by the host–guest complexation with PMCD to efficiently suppress the self-aggregation of TPP cores. Meanwhile, superior to Lys-TPP⊂PMCD complex, the $^1O_2$ generation ability of Gln-TPP greatly increased after complexation with PMCD. These results are in accordance with the distinctive molecular aggregation propensities of two TPP monomers in aqueous solution. It is also noteworthy that compared to PP-NA, the host–guest complexation with PMCD in PR-NW could significantly enhance the $^1O_2$ generation rates and quantum yields of TPP cores, thus highlighting the synergistic effect of enzyme-driven polymerization and host–guest complexation on photodynamic oncotherapy, as described below.

Having confirmed the complexation-enhanced $^1O_2$ generation by the enzymatically cross-linked PR-NW in an inanimate milieu, a qualitative study was conducted to investigate the $^1O_2$ generation using 2′,7′-dichlorodihydrofluorescein diacetate (DCFH-DA) as a cell-permeable fluorescent probe for staining reactive oxygen species (ROS) in cells. Upon coincubation with two biotinylated complex monomers, only faint green fluorescence was detected in 293T cells after light irradiation, while bright green fluorescence was observed in Hela and MCF-7 cells, corresponding to the sufficient ROS production in these two cell lines (Figure 3f).

Subsequently, the cell counting kit-8 (CCK-8) assay reveals that the cell viability remained above 85% after coincubation in dark for 24 h even at a high TPP monomer concentration up to 30 μM (Figure S24, Supporting Information). Upon light irradiation at 420 nm for 5 min, both individual inclusion complexes could cause moderate cytotoxicity in Hela cells (Figure S25, Supporting Information). Comparatively, the photocytotoxicity of cancer cells was significantly enhanced upon coincubation with two biotinylated inclusion complexes (Lys-TPP⊂Bio-PMCD + Gln-TPP⊂Bio-PMCD), whereas a high survival rate was exclusively achieved in normal cells (Figure 3e,g,h). Taking the TPP concentration at 0.5 μM as an example, the relative cellular viability was obtained as high as 70.2% after incubation with the biotinylated inclusion complexes in 293T cells, but they exerted a great cytotoxicity effect, and the corresponding viability was sharply declined to only 7.9% in Hela cells. In addition, the TPP monomers (Lys-TPP + Gln-TPP group) showed undifferentiated cytotoxicity (31.5%) toward 293T cells. Overall, these cytotoxicity results

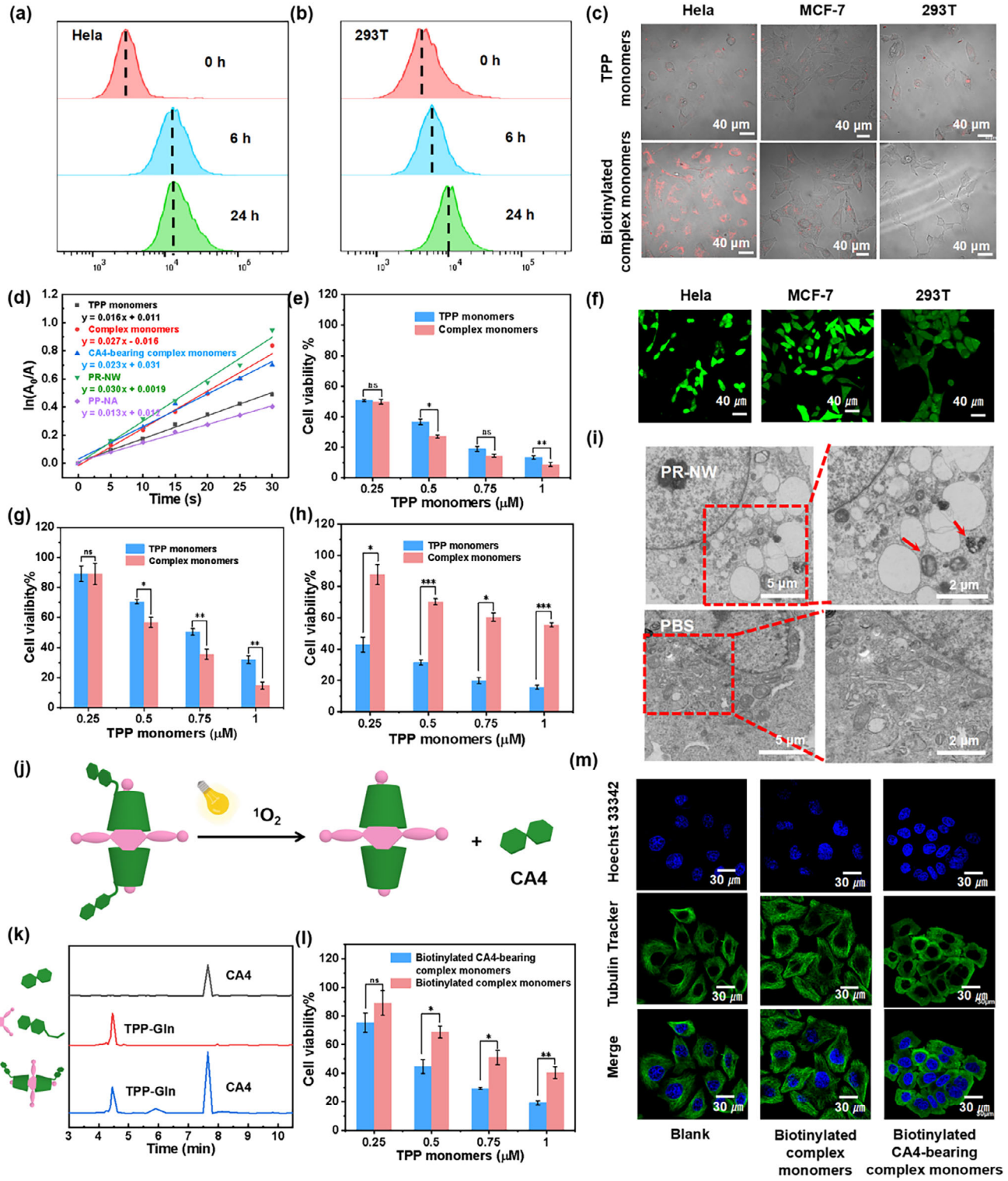

substantiated that the equipment with Bio-PMCD greatly enriched the porphyrin photosensitizers in cancer cells, which could minimize off-target toxicity toward normal cells and maintain potent phototoxicity toward cancer cells.

To further elucidate the mechanism underlying photo-induced cell death, the JC-1 fluorescent probing system was introduced to evaluate the effects of $^1O_2$ generation on mitochondrial membrane potentials. After pre-treatment of Hela cells with two biotinylated complex monomers and followed by light irradiation, CLSM images were collected to verify the relative intensities of JC-1 aggregates (red fluorescence) and monomers (green fluorescence). As can be seen from Figure S26 (Supporting Information), no significant difference in fluorescence signals was observed between irradiated and non-irradiated cells in the blank group. In sharp contrast, the irradiated Hela cells displayed a remarkable green-fluorescence emission enhancement in the group of two complex monomers, accompanied by the characteristic apoptotic morphological alteration with cellular shrinkage. In addition, bio-TEM analysis also revealed that the damaged mitochondria were extensively distributed at the organelle level (Figure 3i). In our case, the incubation with biotinylated inclusion complexes can seriously induce mitochondrial dysfunction under light irradiation, which is responsible for the programmed cell death under oxidative stresses caused by the elevated intracellular ROS level.

By virtue of the chemically modifiable characteristics of CD's skeleton, CA4-PMCD was further synthesized by covalently conjugating the chemotherapeutic agent CA4 through a $^1O_2$-responsive aminoacrylate linker, with the final goal of achieving complexation-enhanced synergistic photodynamic therapy and chemotherapy (Figure 3j). First, the similar $^1O_2$ quantum yields in the cases of TPP@CA4-PMCD and TPP@PMCD complexes demonstrated minimal consumption of $^1O_2$ by the CA4-release process during photoactivation (Figure 3d). Next, high-performance liquid chromatography (HPLC) was exploited to verify the light-activated drug release with and without PMCD. As discerned from Figure 3k, no obvious CA4 was detected using the physical mixture of TPP-Gln and aminoacrylate-bearing CA4 precursor (CA4-OH) upon exposure to light irradiation at 420 nm. Surprisingly, a considerable amount of CA was released from the TPP-Gln⊂CA4-PMCD complex under the same conditions, and the $^1O_2$-triggered drug release promptly proceeded after light irradiation in 30 s. In view of the short half-life of $^1O_2$ in water (≈3.5 µs) and cell (≈0.6 µs), the host–guest complexation with PMCD can not only promote the $^1O_2$ production of TPP cores, but also draw the aminoacrylate and porphyrin sites much closer, which could eventually facilitate intermolecular contact with $^1O_2$ to accelerate the photooxidation process of drug release.[47,48]

Subsequently, the biological impact of the complexation-induced $^1O_2$-responsive drug release on tubular aggregation was further investigated in Hela cells. As shown in Figure 3m, the pristine tubulins stained with the tubulin tracker were uniformly distributed around the nuclei with filament-like structures. Remarkably, after light irradiation for 2 min, closely aggregated tubulins were observed in the selected cell line upon incubation with the biotinylated CA4-bearing inclusion complexes. In addition, control experiments reveal that no significant change was found in microtubule morphology without CA4-PMCD under the same condition. More interestingly, it was found that the in-cellulo formation of polyrotaxanes network could prolong the drug retention after cell feeding by thoroughly replacing culture media; that is, tubulins were largely clustered with each other by the treatment of biotinylated CA4-bearing complexes, whereas the incubation with individual Gln-TPP⊂Bio-PMCD complex could not dramatically change the cytoskeletal structures in cancer cells (Figure S27, Supporting Information). Accordingly, benefitting from the dual synergy of Bio-PMCD and CA4-PMCD, a higher photocytotoxicity was clearly observed in the examined concentration range of TPP monomers from 0.25 to 1 µM (Figure 3l). In addition, CCK-8 assays of free Bio-PMCD and CA4-PMCD under identical conditions showed that Bio-PMCD exhibited negligible cytotoxicity while CA4-PMCD gave moderate cytotoxicity, likely due to the release of CA4 via the photo-induced bond cleavage (Figure S28, Supporting Information).

2.3. Inhibitory Effect of Formed Polyrotaxanes on Cell Dissemination

To shed more light on the role of in-situ polymerization in altering cellular migration behaviors, the wound healing migration assay was also conducted.[49,50] As quantified by Image J analysis of normalized wound areas, PR-NW and PP-NA gave significant anti-migratory effect at 48 h after scratching with a low percentage of wound closure (17% and 30%, respectively). However, Hela cells without any treatment showed an obvious migration healing ability and the wound healing rate reached up to 98%

Figure 3. Flow cytometry results in a) Hela and b) 293T cells incubated with complex monomers for 0, 6, and 24 h; c) CLSM images of two TPP monomers and their biotinylated inclusion complexes with PMCD in Hela, MCF-7, and 293T cells, respectively ([Lys-TPP] = [Gln-TPP] = 5.0 µM and [Bio-PMCD] = 10.0 µM); d) Decomposition rates of ABDA at 378 nm versus light irradiation time by two TPP monomers and their inclusion complexes before and after polymerization. Phototoxicity of two TPP monomers and their biotinylated inclusion complexes in e) Hela g) MCF-7 and h) 293T cells (light power density: 220 mW cm^{-2}, 3 min for Hela cells; 5 min for MCF-7 and 293T cells). f) CLSM images of ROS generation using DCFH-DA as probe in three types of cell lines incubated with biotinylated inclusion complexes ([Lys-TPP] = [Gln-TPP] = 0.5 µM and [Bio-PMCD] = 1.0 µM, light power density: 220 mW cm^{-2}, 5 min). i) Bio-TEM images of Hela cells incubated with biotinylated inclusion complexes and PBS as control (red boxes show zoom areas and red arrows highlight disrupted mitochondria); j) Schematic representation of the PMCD-boosted release of CA4; k) HPLC retention time of CA4, TPP-Gln, and CA4-OH mixture, and TPP-Gln⊂CA4-PMCD complex ([Gln-TPP] = 10 µM, and [CA4-PMCD] = [CA4-OH] = 20 µM). The detection wavelength in each trace was set as 254 nm; l) Phototoxicity of two TPP monomers and their biotinylated CA4-bearing inclusion complexes in Hela cells ([Lys-TPP] = [Gln-TPP] = 0.5 µM and [CA4-PMCD] = 1.0 µM, light power density: 220 mW cm^{-2}, 2 min); m) CLSM images of Hela cells incubated with PBS, biotinylated inclusion complexes, and biotinylated CA4-bearing inclusion complexes, respectively ([Lys-TPP] = [Gln-TPP] = 0.25 µM, [Bio-PMCD] = 0.7 µM, and [CA4-PMCD] = 0.3 µM, light power density: 220 mW cm^{-2}, 30 s). Data denote mean ± S.D. (n = 3). ns $p > 0.05$, $^*p < 0.05$, $^{**}p < 0.01$, $^{***}p < 0.001$.

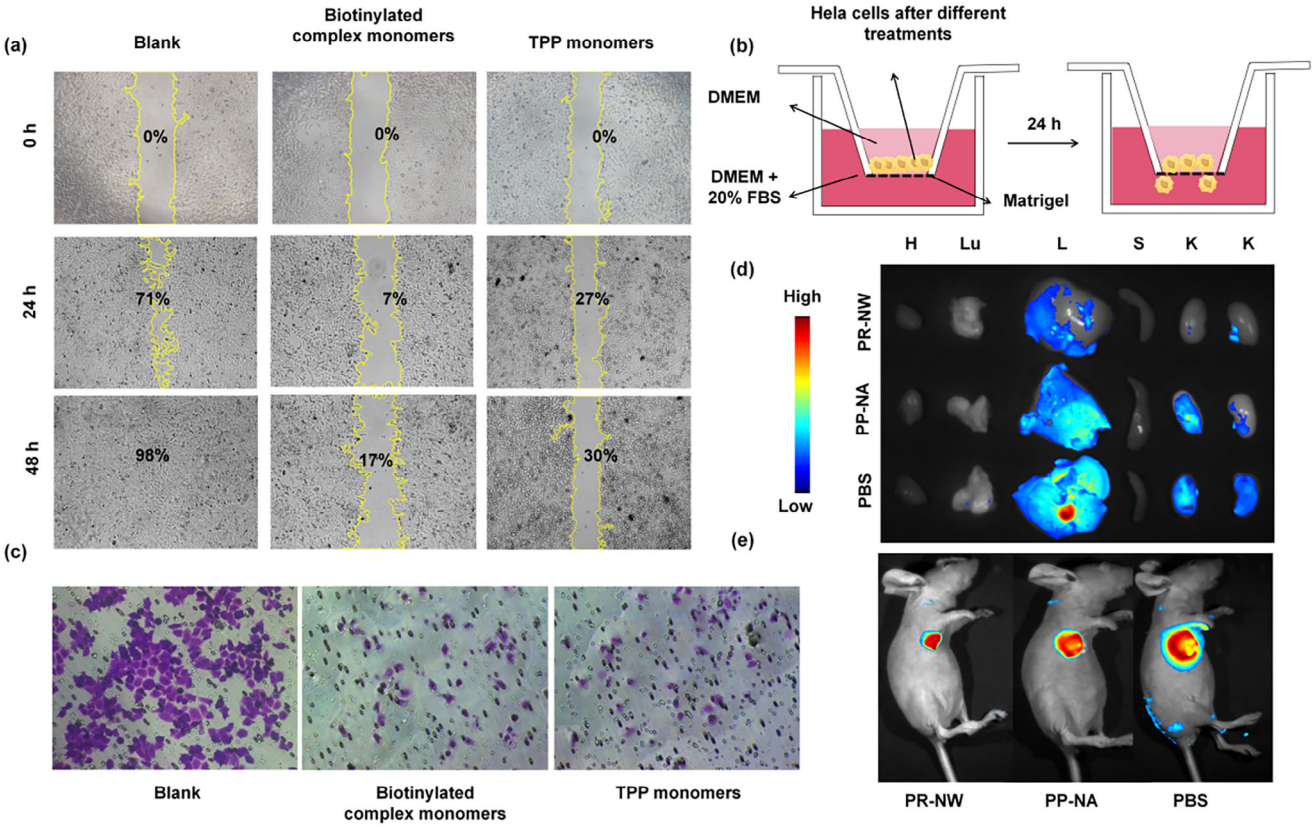

Figure 4. a) Microscopic images of wound healing of Hela cells upon incubation with PBS, TPP monomers, and complex monomers; b) Schematic illustration of cell transwell assays to evaluate cell invasion ability; c) Representative images of Hela cells incubated with PBS, TPP monomers, and complex monomers for 24 h in transwell assay; d) Biodistribution of GFP-labeled Hela cells in major organs and e) tumor volume changes after local administration of PBS, PR-NW, and PP-NA at tumor sites on day #7 (H, Lu, L, S, and K stand for heart, lung, liver, spleen, and kidney, respectively). Data denote mean ± S.D. ($n = 3$).

(**Figure** 4a). Meanwhile, a transwell assay was conducted to explore the longitudinal invasion capacities of Hela cells after different treatments (Figure 4b). Compared to PBS as a control, the invasion capacity of Hela cells through Matrigel as the extracellular matrix on top of the porous membrane was largely inhibited after treatment by PR-NW and PP-NA (Figure 4c).

To further validate the inhibitory effect on cancer cell dissemination in the animal body, a tumor-bearing mouse model was established using the green fluorescent protein (GFP)-labeled Hela cells. Local administration of three formulations (PR-NW, PP-NA, and PBS) was performed at the tumor site every 3 days after tumor implantation. The ex vivo fluorescence images revealed strikingly distinct biodistribution patterns; that is, on day #7, PR-NW showed weak fluorescence signals exclusively in liver, while PP-NA and PBS induced substantial hepatic–renal metastasis (Figure 4d). As a result, benefitting from the exceptional suppression of cell migration at both cell and animal levels, tumor growth was greatly inhibited with minimal tumor volume changes (Figure 4e). These findings jointly demonstrate that PR-NW could significantly inhibit cancer cell dissemination, which is mainly contributed to its larger surface area and specific cell selectivity of biotinylated polymerizable inclusion complexes in polyrotaxane network.

2.4. In Vivo Application of Formed Polyrotaxanes for Tissue Targeting and Phototherapy

Prior to the in vivo evaluation of the polyrotaxane network on combined phototherapy, the tissue-targeting specificity and retention prolongation at the tumor site were initially explored. After intravenous administration of the two biotinylated inclusion complexes, the formed PR-NW was predominantly accumulated in tumor tissues with minimal off-target fluorescence, while the nonspecific TPP derivatives showed systemic distribution in the tumor-bearing BALB/c nude mice (**Figure** 5b). Moreover, to visualize the tumor-targeting specificity and retention duration of the in-situ formed polyrotaxanes, the biodistribution in mice was monitored by in vivo fluorescence imaging at periodic intervals by intravenous injection via the tail vein. The administration of biotinylated inclusion complexes exhibited concentrated red fluorescence exclusively in tumor region at 24 h post-injection. In the tumor-bearing mice xenografted by TGase-overexpressing HeLa cells, persistent red fluorescence at tumor sites was clearly observed up to 120 h post-administration. In contrast, the one by TGase-deficient MCF-7 cells showed complete fluorescence disappearance within 48 h, demonstrating a rapid metabolic clearance in the absence of TGase-mediated

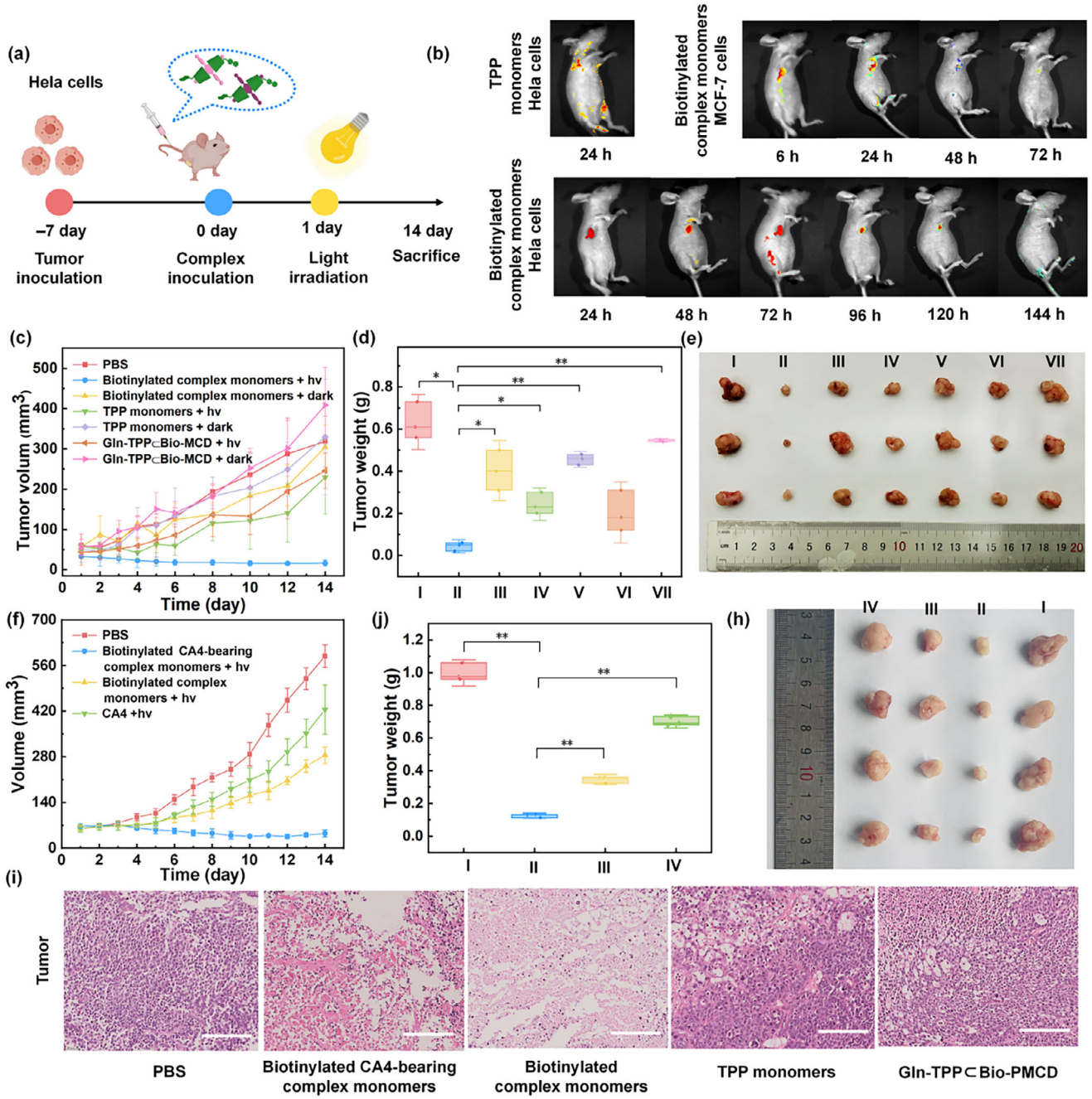

Figure 5. a) Schematic illustration of the establishment of the tumor model in mice and the tail vein injection of the drug; b) Tissue targeting and retention time in tumor-bearing mice with MCF-7- and Hela-derived xenograft; Changes in c,f) tumor volumes and d,j) tumor weights of the mice in different groups during 14-day treatment; e,h) Representative photographs of tumors in different groups on day #14. (I: PBS, II: biotinylated complex monomers + hν, III: biotinylated complex monomers + dark, IV: TPP monomers + hν, V: TPP monomers + dark, VI: Gln-TPP⊂Bio-PMCD complex + hν, VII: Gln-TPP⊂Bio-PMCD complex + dark in d and e; I: PBS, II: biotinylated CA4-bearing complex monomers + hν, III: biotinylated complex monomers + hν, IV: CA4 in j,h); and i) H&E staining images of tumor-bearing nude mouse treated by different samples sacrificed on day #14. The scale bars are 200 μm. Data denote mean ± S.D. ($n = 3$). $^{*}p < 0.05$, $^{**}p < 0.01$.

polymerization. This observation aligned with our findings from the confocal microscopy experiments, in which HeLa cells maintained the pronounced red fluorescence of porphyrin after 72 h in fresh medium, whereas MCF-7 cells showed negligible fluorescence signals at the same time point (Figure S29, Supporting Information). Overall, these results substantiate that the enzymatic polymerization could significantly enhance tumor retention duration through the in-situ formation of polyrotaxane network.

Motivated by the complexation-enhanced ROS generation, photoactivated drug release, and inhibition on cancer cell

dissemination, the therapeutic outcomes of intracellularly polymerized polyrotaxane networks were further examined in murine models (Figure 5a). Under such circumstances, given the relatively higher cytotoxicity of Gln-TPP⊂Bio-PMCD complex than its Lys-TPP counterpart, the former complex was selected as a non-polymeric control for subsequent evaluation on in vivo antitumor efficacy. Meanwhile, benefitting from the targeted tumor accumulation and enhanced ROS generation, remarkable tumor regression was achieved upon the formation of biotinylated PR-NW under light irradiation on day #14; in contrast, exponential tumor volume expansion was observed in other experimental groups (Figure 5c–e). Finally, the combined therapeutic effect in mice was further evaluated after the introduction of CA4-PMCD. Although tumor growth was greatly suppressed by the treatment of biotinylated inclusion complex, the presence of CA4-PMCD gave the best curative effect by the combination of targeted photodynamic and photoactivable chemotherapeutic treatments (Figure 5f-h). In addition, as shown in Figures S30 and S31 (Supporting Information), the body weights in all experimental groups were stably maintained throughout the 14-day observation period, implying the favorable biosafety profiles of TPP derivatives, PP-NA, and PR-NW. Accordingly, hematoxylin and eosin (H&E) staining of tumor tissues and key organs was conducted (Figure 5i; Figures S32 and S33, Supporting Information). Among all the examined groups, the most significant cell apoptosis/death was observed in tumors, and meanwhile, no discernible pathological alteration or tissue damage was observed in the treatment groups of TPPs and their complex monomers.

3. Conclusion

In conclusion, the selective biosynthesis of polyrotaxane assemblies in living cells was first realized via the TGase-triggered coupling reaction for combinational cancer therapy. Spectroscopic and microscopic studies revealed that the inclusion complexation of PMCD with Lys-TPP and Gln-TPP could greatly enhance the structural rigidity and integrity, thereby leading to morphological conversion from amorphous aggregates to regular 2D networks. Moreover, by leveraging the macrocyclic confinement for molecular segregation and conformational fixation, the TPP cores were constrained in the PMCD's cavity and the photophysical pathway of photosensitive fluorophores revived to dramatically augment the efficiencies of both fluorescence emission and $^1O_2$ yield. After equipment of the biotinylated PMCD, the discrete host–guest complexes could be selectively self-assembled into polyrotaxane networks in cancer cells. The complexation-enhanced $^1O_2$ production could further promote the self-photocleavage of aminoacrylate linker and the release of CA4 drug. This leads to the significant cytotoxicity toward the cancer cells through inducing cytoskeleton destruction and mitochondrial dysfunction. In vivo studies in the murine model confirmed the chemo-photodynamic therapeutic efficacy of the in-situ formed polyrotaxane networks to efficiently inhibit tumor growth and metastases with satisfactory biosafety issues. To be envisioned, our work featuring the enzyme-triggered intracellular biosynthesis of polyrotaxane assemblies will enrich the toolbox of function-oriented topologically complex supramolecules and expedite the development of precise and personalized supramolecular nanomedicines in the future.

4. Experimental Section

General Methods and Materials: ^1H and ^{13}C NMR spectra were recorded through a Bruker AV400 instrument in the indicated solvents at 25 °C. Dynamic light scattering (DLS) experiments were conducted on a DynaPro NanoStar DLS detector. UV–vis data were collected on a Shimadzu UV-3600 spectrophotometer. Fluorescent measurements were performed on a JASCO FP-750 spectrometer. The Zeta potentials were examined on a Brookhaven ZETAPALS/BI-200SM at 25 °C. Transmission electron microscopic (TEM) images were recorded on FEI Tecnai G2 F20 under 200 kV. X-ray photoelectron spectroscopy (XPS) was conducted on Kratos Analytical Ltd (Axis Ultra DLD). Atomic force microscope (AFM) were conducted on Bruker Dimension Icon. Gel permeation chromatography (GPC) was conducted on DAWN HELEOS 8+. The confocal laser scanning microscopic (CLSM) imaging experiments were conducted with a Zeiss LSM880 instrument. The flow cytometric experiments were conducted with NoVoCyte 2060R Agilent Technologies. In vivo imaging was carried on CRi Maestro.

Cell Lines and Animals: Human cervical cancer cells (Hela), human breast cancer cells (MCF-7), and human renal epithelial (293T) cells were obtained from the cell bank of the Chinese Academy of Sciences. Hela cells and MCF-7 cells were cultured in DMEM high glucose medium (Gibco), containing 10% fetal bovine serum (FBS) at 37 °C in a 5% CO_2 humidified environment incubator (Thermo Scientific, USA).

Animals and Ethical Statement: BALB/c nude mice for tumor suppression assessment in vivo were purchased from Beijing FHK Bioscience Co. Ltd. All the animals were acclimated under standard laboratory conditions, including a ventilated room, a suitable temperature (25 ± 1 °C), controlled humidity (60 ± 5%), and a 12 h light/dark cycle. All procedures were conducted in accordance with the "Guiding Principles in the Care and Use of Animals" (China) and also assessed by the Animal Experimentation Ethics Committee of Nankai University, and the assigned approval number is 2021- SYDWLL-000079.

Detection of In Vitro ROS Yields of Different Components: Commercial 9,10-anthracenediyl-bis (methylene)dimalonic acid (ABDA) was utilized as a tracer agent to assess the differences in $^1O_2$ production efficiencies among various samples. Specifically, each sample and ABDA were dispersed together in 3 mL of deionized water, with final concentrations of 10 and 50 µM, respectively. Subsequently, the mixed solution was irradiated with white light (>420 nm) at a power of 220 mW cm^{-2}. The efficiency of $^1O_2$ generation was measured by monitoring the UV–vis absorbance change of ABDA at 378 nm at different irradiation time intervals. Rose Bengal (RB) was used as a standard for evaluating the $^1O_2$ quantum yield of photosensitizers (Φ_{PS}), which could be calculated by the following Equation (1).

$$\Phi_{PS} = \Phi_{RB} \frac{k_{PS}/k_{RB}}{A_{PS}/A_{RB}} \quad (1)$$

where k_{PS} and k_{RB} represent the decomposition rate constants of ABDA with photosensitizers (PS) and RB, respectively. A_{PS} and A_{RB} represent the integration areas of PS and RB under the absorption band in the wavelength range above 420 nm. Φ_{RB} is a known constant with a value of 75%.

Determination of Aggregation Constant (K_{agg}): The value of K_{agg} is calculated by Equation (2). In Equation (2), ε denotes the apparent extinction coefficient obtained from the spectra; ε_f and ε_a are the extinction coefficients for the free and the aggregated species, respectively; K_{agg} is the aggregation constant; and c is the total TPP concentration in the sample.

$$\varepsilon\,(c) = \frac{2K_{agg}c + 1 - \sqrt{4Kc + 1}}{2{K_{agg}}^2c^2}(\varepsilon_f - \varepsilon_a) + \varepsilon_a \quad (2)$$

Flow Cytometry Assay: Flow cytometry experiments were conducted to compare the cellular uptake efficiency of Lys-TPP⊂Bio-PMCD and Gln-TPP⊂Bio-PMCD complexes between cancer cell lines (Hela and MCF-7) and normal cells (293T). Cells were seeded at 5×10^5 cells per well in a 24-well plate and further cultured for 24 h. Then, following incubating for 0, 6, and 24 h, followed by flow cytometry assay in PC5.5 channel.

Confocal Laser Scanning Microscopy (CLSM): To observe the internalization of the assemblies, Hela, MCF-7, and 293T cells plated in confocal dishes were co-incubated with Lys-TPP + Gln-TPP, Lys-TPP⊂Bio-PMCD and Gln-TPP⊂Bio-PMCD, respectively, for 12 h. Subsequently, the cells were treated with PBS, then examined through confocal laser scanning microscopy (CLSM, Olympus, FV1000).

In Vitro Cytotoxicity Tests: The cytotoxicity of assemblies or photosensitizers to normal cells (293T cells) and tumor cells (Hela and MCF-7 cells) in light or dark conditions was determined by the CCK-8 assay. Initially, Hela, MCF-7, or 293T cells were plated in 96-well plates at a density of 5×10^3 cells per well. After 24 h of incubation, the original medium was replaced by samples at different concentrations. ≈12 h later, after replacing with fresh culture medium, each well was irradiated with light for 5 min (420 nm, 220 mW cm^{-2}). Following an additional hour of incubation, the medium was replaced with fresh culture medium containing 10% CCK-8, and the cells were further incubated at 37 °C and 5% CO_2 for 4 h. Finally, a microplate reader (ALL SHENG, AMR-100) was used to measure the absorbance of the plates at 450 nm to evaluate cell viability.

To further expand the system's functionality, CA4-PMCD was subsequently introduced for synergistic chemo-photodynamic combination therapy. While maintaining identical experimental conditions, the light irradiation duration was strategically reduced to 2 min due to considerations of enhanced toxicity profiles, thereby enabling systematic evaluation of its phototoxic effects.

Wound Healing Assay: For the wound healing assay, Hela cell monolayers were established by seeding in 6-well culture plates and allowing cellular adhesion for 24 h until achieving 80–90% surface confluency. Then the confluent cell monolayers were wounded with a P200 pipet tip, and cells were washed with PBS repeatedly and incubated with PP-NA and PR-NW at a concentration of 10 μM for another 24 and 48 h. The wound healing area was photographed under a microscope. Quantitative analysis of migratory capacity was conducted through digital image processing (Image J) by measuring wound margin retraction distances relative to baseline measurements.

Statistical Analysis: Statistical analyses were performed using Origin and SPSS software. Statistical data denote mean ± S.D. unless otherwise noted. Details of the statistical tests performed, *P* values, and the number of replicates were provided in the figure legends. A threshold for significance of $p < 0.05$ was used for all experiments. A *p*-value ≤ 0.05 was considered statistically significant, dubbed as $^{*}p \leq 0.01$ was dubbed as **, and $p \leq 0.001$ was dubbed as ***, $p > 0.05$ (non-significant) was dubbed as ns.

Supporting Information

Supporting Information is available from the Wiley Online Library or from the author.

Acknowledgements

This work was financially supported by the National Natural Science Foundation of China (22171148, 22371148, and 22131008), Haihe Laboratory of Sustainable Chemical Transformation, and the Fundamental Research Funds for the Central Universities (Nankai University).

Conflict of Interest

The authors declare no conflict of interest.

Data Availability Statement

The data that support the findings of this study are available in the supplementary material of this article.

Keywords

host-guest chemistry, polyrotaxane, photosensitization, in-cellulo assembly, supramolecular phototherapy

Received: September 23, 2025
Revised: October 19, 2025
Published online: November 3, 2025

[1] D. Wu, J. Lei, Z. Zhang, F. Huang, M. Buljan, G. Yu, *Chem. Soc. Rev.* **2023**, *52*, 2911.
[2] P. Laskar, O. P. Varghese, V. P. Shastri, *Adv. Nano. Biomed. Res.* **2023**, *3*, 2200174.
[3] Y. Che, M. Zuo, Y. Che, P. Yu, X. Chen, X. Zhang, *Nat. Commun.* **2023**, *14*, 5229.
[4] A. Zhang, S. Zhao, J. Tyson, K. Deisseroth, Z. Bao, *Nat. Synth.* **2024**, *3*, 943.
[5] O. Baghdasaryan, S. Khan, J.-C. Lin, J. Lee-Kin, C.-Y. Hsu, C.-M. J. Hu, C. Tan, *Trends Biotechnol.* **2024**, *42*, 241.
[6] A.-A. Liu, E.-Z. Sun, Z.-G. Wang, S.-L. Liu, D.-W. Pang, *Natl. Sci. Rev.* **2022**, *9*, 162.
[7] S. Kim, G. Park, D. Kim, M. S. Hasan, C. Lim, M. S. Seu, J. H. Ryu, *Adv. Nano. Biomed Res.* **2024**, *4*, 2300137.
[8] J. Geng, W. Li, Y. Zhang, N. Thottappillil, J. Clavadetscher, A. Lilienkampf, M. Bradley, *Nat. Chem.* **2019**, *11*, 578.
[9] D. Schauenburg, T. Weil, *Adv. Sci.* **2024**, *11*, 2303396.
[10] K. Parkatzidis, H. S. Wang, N. P. Truong, A. Anastasaki, *Chem* **2020**, *6*, 1575.
[11] Z. Zhou, K. Maxeiner, D. Y. W. Ng, T. Weil, *Acc. Chem. Res.* **2022**, *55*, 2998.
[12] F. Gao, L. Zhu, L. Jiang, J. Zhang, S. Ji, W. Gao, G. Ma, Y. Chang, X. Ma, Y. Guo, *Adv. Funct. Mater.* **2024**, *34*, 2312182.
[13] T. Liu, M. Zhu, X. Chang, X. Tang, P. Yuan, R. Tian, Z. Zhu, Y. Zhang, X. Chen, *Adv. Mater.* **2023**, *35*, 2300086.
[14] D. Zhang, X. Hou, D. Pan, Z. Li, Q. Gong, K. Luo, *Adv. Mater.* **2024**, *36*, 2403588.
[15] X. Wang, M. Li, Y. Huo, Y. Li, X. Yao, C. Xue, Y. Fei, Y. Xiang, K. Cai, Y. Zhao, Z. Luo, *Adv. Funct. Mater.* **2020**, *30*, 2000229.
[16] G. Qi, X. Liu, L. Shi, M. Wu, J. Liu, B. Liu, *Adv. Mater.* **2022**, *34*, 2106885.
[17] S.-Y. Dai, Z. Xiao, F. Shen, I. Lim, J. Rao, *J. Am. Chem. Soc.* **2025**, *147*, 2037.
[18] R. Zhang, P. Hu, Y. Xu, Z. Wang, D. Yang, C. Yao, *CCS Chem* **2024**, *6*, 1557.
[19] L. Cui, S. Vivona, B. R. Smith, S. R. Kothapalli, J. Liu, X. Ma, Z. Chen, M. Taylor, P. H. Kierstead, J. M. J. Frechet, S. S. Gambhir, J. Rao, *J. Am. Chem. Soc.* **2020**, *142*, 15575.
[20] X. Q. Yang, C. H. Xu, X. Zhang, P. Li, F. Y. Sun, X. Y. Liu, X. Y. Wang, R. T. K. Kwok, J. L. Yang, J. W. Y. Lam, Y. Y. Liang, B. Z. Tang, *Adv. Funct. Mater.* **2023**, *33*, 2300746.
[21] D. Liu, M. Lin, L. Shu, J. Sun, X. Chen, *Nano Lett.* **2023**, *23*, 5713.
[22] Y. Dai, T. Li, Z. Zhang, Y. Tan, S. Pan, L. Zhang, H. Xu, *J. Am. Chem. Soc.* **2021**, *143*, 10709.
[23] Z. Cui, R. Ji, J. Xie, C. Wang, J. Tian, W. Zhang, *Biomacromolecules* **2024**, *25*, 2302.
[24] R. B. Grubbs, R. H. Grubbs, *Macromolecules* **2017**, *50*, 6979.

[25] H. He, W. Tan, J. Guo, M. Yi, A. N. Shy, B. Xu, *Chem. Rev.* **2020**, *120*, 9994.
[26] W. Tan, Q. Zhang, J. Wang, M. Yi, H. He, B. Xu, *Angew. Chem., Int. Ed.* **2021**, *60*, 12796.
[27] J. Liu, B. Liu, *Prog. Polym. Sci.* **2022**, *129*, 101545.
[28] M. Zhu, S. Wang, Z. Li, J. Li, Z. Xu, X. Liu, X. Huang, *Nat. Commun.* **2023**, *14*, 3598.
[29] J. Ning, Z. Sun, R. Hübner, H. Karring, M. F. Ebbesen, M. Dimde, C. Wu, *Nat. Catal.* **2024**, *7*, 1404.
[30] M. Bienz, *Cell* **2020**, *182*, 799.
[31] Q. Cui, X. Zhang, *Chin. J. Chem.* **2023**, *41*, 2715.
[32] L. Chen, X. Sheng, G. Li, F. Huang, *Chem. Soc. Rev.* **2022**, *51*, 7046.
[33] H. Masai, Y. Oka, J. Terao, *Chem. Commun.* **2022**, *58*, 1644.
[34] Z. Liu, L. Ye, J. Xi, J. Wang, Z. Feng, *Prog. Polym. Sci.* **2021**, *118*, 101408.
[35] C. Xu, Y.-L. Wu, Z. Li, X. J. Loh, *Mater. Chem. Front.* **2019**, *3*, 181.
[36] A. Tamura, N. Yui, *Chem. Commun.* **2014**, *50*, 13433.
[37] T. Highasi, K. Motoyama, H. Arima, *J. Drug Delivery Sci. Technol.* **2013**, *23*, 523.
[38] J.-J. Li, F. Zhao, J. Li, *Appl. Microbiol. Biotechnol.* **2011**, *90*, 427.
[39] S. Paryente, H. Aledwan, A. Saady, *Commun. Chem.* **2025**, *8*, 149.
[40] T. Higashi, T. Taharabaru, K. Motoyama, *Carbohydr. Polym.* **2024**, *337*, 122143.
[41] R. Du, T. Bao, D. Kong, Q. Zhang, X. Jia, *ChemPlusChem* **2024**, *89*, 202300706.
[42] A. Puglisi, Y. Yagci, *Macromol. Rapid Commun.* **2019**, *40*, 1800557.
[43] Z. Li, C. J. Zeman VI, S. Valandro, J. P. O. Bantang, K. S. Schanze, *Molecules* **2023**, *28*, 4115.
[44] V. Villari, N. Micali, A. Nicosia, P. Mineo, *Top Curr. Chem.* **2021**, *379*, 35.
[45] L.-L. Li, S.-L. Qiao, W.-J. Liu, Y. Ma, D. Wan, J. Pan, H. Wang, *Nat. Commun.* **2017**, *8*, 1276.
[46] E. Ornati, J. Perrard, T. A. Hoffmann, R. Bonon, N. Bruns, *J. Am. Chem. Soc.* **2025**, *147*, 9496.
[47] M. Bregnhoj, M. Westberg, F. Jensen, P. R. Ogilby, *Phys. Chem. Chem. Phys.* **2016**, *18*, 22946.
[48] Y. Zhai, X. Huang, K. Zhang, Y. Huang, Y. Jiang, J. Cui, Z. Zhang, C. K. C. Chiu, W. Zhong, G. Li, *Nat. Commun.* **2022**, *13*, 4906.
[49] G. Gao, Y.-W. Jiang, W. Zhan, X. Liu, R. Tang, X. Sun, Y. Deng, L. Xu, G. Liang, *J. Am. Chem. Soc.* **2022**, *144*, 11897.
[50] Q. Yu, Y.-M. Zhang, Y.-H. Liu, X. Xu, Y. Liu, *Sci. Adv.* **2018**, *4*, aat2297.